# Thermal transport in ZnO nanocrystal networks synthesized by nonthermal plasma

Xuewang Wu,[1] Benjamin L. Greenberg,[1] Yingying Zhang,[1] Jacob T. Held ◎,[2] Dingbin Huang ◎,[1] Javier G. Barriocanal,[3]
K. Andre Mkhoyan ◎,[2] Eray S. Aydil ◎,[4] Uwe Kortshagen ◎,[1] and Xiaojia Wang[1,*]

[1]*Department of Mechanical Engineering, University of Minnesota, Twin Cities, Minneapolis, Minnesota 55455, USA*
[2]*Department of Chemical Engineering and Material Science, University of Minnesota, Twin Cities, Minneapolis, Minnesota 55455, USA*
[3]*Characterization Facility, University of Minnesota, Twin Cities, Minneapolis, Minnesota 55455, USA*
[4]*Department of Chemical and Biomolecular Engineering, New York University Tandon School of Engineering,
Brooklyn, New York 11201, USA*

Semiconductor materials with independently controlled electrical and thermal properties have a unique promise for energy-related applications from thermoelectrics and thermophotovoltaics. Here, using nonthermal plasma synthesized, direct-contact zinc oxide (ZnO) nanocrystal (NC) networks infilled with amorphous $Al_2O_3$, and amorphous $ZnO$-$Al_2O_3$ mixture, it is shown that such independent control of electrical and thermal properties is achievable. In this study, in addition to our early reports on control of the electrical properties in these two-phase nanocomposites by tailoring the contact radius between NCs, we demonstrate that the infill composition has a significant impact on the overall thermal conductivity of the NC network and can be used for thermal control. It is also shown that in these heterogeneous systems, the phonons are the dominant heat carriers, and the NC-NC contact radius has a negligible effect on thermal transport. The work suggests that this paradigm of independently controlling the electrical and thermal properties of NC-based materials through tuning the NC-NC contact radius and infill composition can be exploited even further by varying NC and infill materials with potential applications ranging from solar cells and light emitting diodes to solid-state energy converters.

## I. INTRODUCTION

Independent control of the electrical and thermal properties of semiconductors is of great interest for thermoelectric power generation and refrigeration, and for many electronic applications, such as vertical cavity surface emitting lasers [1]. Significant progress has been made through nanostructuring of materials, for instance, through ball milling and consolidation by hot pressing or spark plasma sintering, to achieve size confinement for phonon transport without affecting electronic transport [2–6]. While nanostructuring of materials allows controlled reduction of thermal conductivity without significant loss of electrical conductivity, the approach has been limited to only a few materials and compositions. Here, we present an alternative approach for independent control of electrical and thermal properties of composite materials comprising a network of semiconductor nanocrystals (NCs). Such NCs have already stimulated a wide range of applications due to their size-dependent electrical and optical properties [7–11] for solar cells [12,13], light emitting diodes (LEDs) [14,15], field-effect transistors [16,17], and thermoelectric generators [18,19].

Our approach is based on a two-phase system, where one phase (ZnO NCs) controls electrical properties, and the second phase (amorphous alumina, a:$Al_2O_3$) fills the void space between NCs and controls thermal properties. Such a dense two-phase NC network can be assembled by depositing a NC film on the substrate of choice and infilling the spaces between NCs with a:$Al_2O_3$ via atomic layer deposition (ALD) [20–24]. Nonthermal plasma synthesized NCs are particularly well suited for this approach, as they are solvent- and ligand-free [25], enabling the formation of dense NC networks by direct gas-phase deposition. Unlike most NC networks produced by colloidal synthesis, in which thermal properties are often controlled by organic ligands [26–30], NC networks from plasma synthesis feature NCs in direct contact with each other and intimate contact can be achieved without ligand exchange or removal [20,22,23,31]. In our prior studies, we showed that electronic transport in these plasma synthesized NC networks can be controlled from insulating to metallic via tuning of the inter-NC contact area (as described by the contact radius $\rho$) and the carrier concentration ($n$) [23,32]. The thermal transport properties of such heterogeneous nanocomposites have not been studied, however, despite the fact that they play an important role in various NCs-based applications, such as the thermal management and lifetime of NC-based LEDs, and the efficiency of thermoelectric devices.

To close this knowledge gap, we explore the thermal transport in these heterogeneous nanocomposites comprising ZnO NCs and a:$Al_2O_3$ infill through experiments and modeling. We systematically vary the contact radius between NCs ($\rho$), the carrier concentration ($n$), and the infill composition to examine thermal transport properties experimentally. We apply a modified effective medium approximation (EMA) model to frame our experiments and reveal the influences of various factors on thermal transport in these NC networks. These factors include $\rho$, the volumetric fraction of NCs ($\varepsilon_{NC}$),
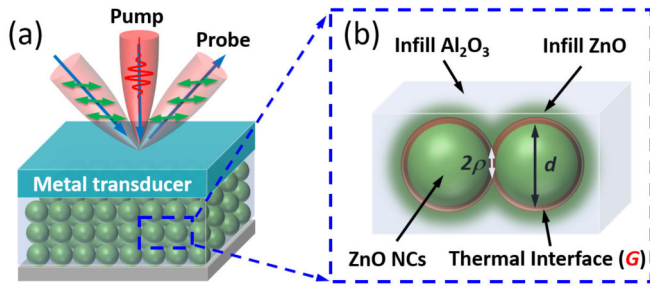
*Corresponding author: wang4940@umn.edu

FIG. 1. (a) Schematic of ZnO NC networks for thermal characterization. A metal transducer layer (Al) is deposited on the top surface of each sample for time-domain thermoreflectance measurement. (b) Cross-sectional sketch of two NCs in contact through facets with radius $\rho$. ZnO and $Al_2O_3$ are coated on NC surface from inside to outside in sequence by ALD to serve as infill materials. The interface between the NC and infill material is highlighted as orange. The nanocrystal diameter $d$ is controlled to be ~10 nm.

the NC thermal conductivity ($\Lambda_{NC}$), the interfacial thermal conductance ($G$) between NCs and infill materials, and the infill matrix thermal conductivity ($\Lambda_{IF}$). The model allows us to predict the thermal properties of our nanocomposite materials in a range broader than what could be explored with current experiments. To facilitate the discussion, we provide a list of important parameters in Sec. S1 of the Supplemental Material [33].

## II. SAMPLE INFORMATION

### A. Sample synthesis and characterization

ZnO NC networks (Fig. 1) were prepared via nonthermal plasma synthesis [34] and inertial impact deposition [35–37] on borosilicate substrates. These networks were infilled with ZnO and/or $Al_2O_3$ via ALD, sintered, and photodoped by intense pulsed light (IPL) exposure. The details of synthesis, deposition, infilling, sintering, and photodoping procedures have been described previously [20,23]. Briefly, after synthesis and deposition of ZnO NCs onto a substrate, the inter-

NC contact radius and electron density are controlled by a combination of IPL pulses that partially sinter the network, followed by ALD infilling and IPL pulses that photodope the NCs. The IPL sequences are distinguished as "sintering IPL" and "doping IPL."

The $Al_2O_3$ ALD infilling conditions were the same for all samples, while the ZnO ALD, sintering IPL, and doping IPL treatments were varied by design (Table I). The $Al_2O_3$ infill removes electron-trapping surface OH and increases the number of free electrons per NC from ≪1 to ~10, which translates to a free-electron density of $n \approx 10^{19}$ cm$^{-3}$ [20]. Sintering IPL increases electrical conductivity $\sigma$ by increasing the inter-NC contact radius $\rho$ [Fig. 1(b)], and doping IPL further increases $\sigma$ by increasing $n$ [23]. ZnO ALD also increases $\sigma$ by further improving $\rho$ [38]. For reference, we also deposited $Al_2O_3$ films on monocrystalline ZnO substrates along different crystal orientations, i.e., (0001), (1$\bar{1}$00), and (11$\bar{2}$0). NCs were infilled using over 2700 rapid-ALD cycles at 180 °C: in rapid ALD the precursor (trimethylaluminum and water) pulse and purge times were 0.015 and 5 s, respectively. The structural and surface features of the NC networks were characterized with scanning transmission electron microscopy (STEM), atomic force microscopy (AFM), and x-ray diffraction (XRD). Details regarding the sample characterization methods are provided in the Experiment section.

### B. Structural characteristics of ZnO NC thin films

The sample information is summarized in Table I. The film thickness of ZnO NCs obtained from ellipsometry is 300 ± 20 nm. For all samples, the volumetric fraction of ZnO NCs ($\varepsilon_{NC}$) is measured to be 33 ± 2%, via ellipsometry and Bruggeman effective-medium approximation. We estimate that a pore volume fraction ($\varepsilon_p$) of 5% remains after infilling with ALD, based on the dependence of porosity on the number of ALD infill cycles [20]. The infill ZnO and infill $Al_2O_3$ volume fractions, $\varepsilon_{IF,ZnO}$ and $\varepsilon_{IF,Al_2O_3}$, respectively, vary with the number of ZnO-infill ALD cycles. For series 1–3, the cycles of ZnO infill increase from 0 to 32, and the corresponding $\varepsilon_{IF,ZnO}$ increase from 0 to 47%, while $\varepsilon_{IF,Al_2O_3}$ decrease from 62% to 15%, as shown in Table I.

TABLE I. Sample information of ZnO NC networks with a NC diameter $d$ of 9.4 nm.

| Series | Sample no. | Number of sintering light pulses[a] | Number of doping light pulses[b] | Infill by ALD | Volumetric fraction $\varepsilon$ | | | |
| --- | --- | --- | --- | --- | --- | --- | --- | --- |
| | | | | | ZnO NC | $Al_2O_3$ infill | ZnO infill | Porosity |
| | 1-*m*-0 (*m* = 0–1000) | *m* | 0 | | | | | |
| 1 | 1-1000-*n* (*n* = 0–1000) | 1000 | *n* | 70 cycles of a:$Al_2O_3$ | 33% | 62% | 0 | 5% |
| | 1-a[c] | 1000 | 0 | | | | | |
| | 1-b[c] | 1000 | 1000 | | | | | |
| 2 | 2-a | 1000 | 0 | 8 cycles of ZnO + 70 cycles of a:$Al_2O_3$ | 33% | 48% | 14% | 5% |
| | 2-b | 1000 | 1000 | | | | | |
| 3 | 3-a | 1000 | 0 | 32 cycles of ZnO + 70 cycles of a:$Al_2O_3$ | 33% | 15% | 47% | 5% |
| | 3-b | 1000 | 1000 | | | | | |

[a]The number of sintering light pulses is the number of IPL flashes before ALD of infill materials.
[b]The number of doping light pulses is the number of IPL flashes after ALD of infill materials.
[c]Samples labeled as 1-a and 1-b are the same ones as those labeled as 1-1000-0 and 1-1000-1000, respectively.
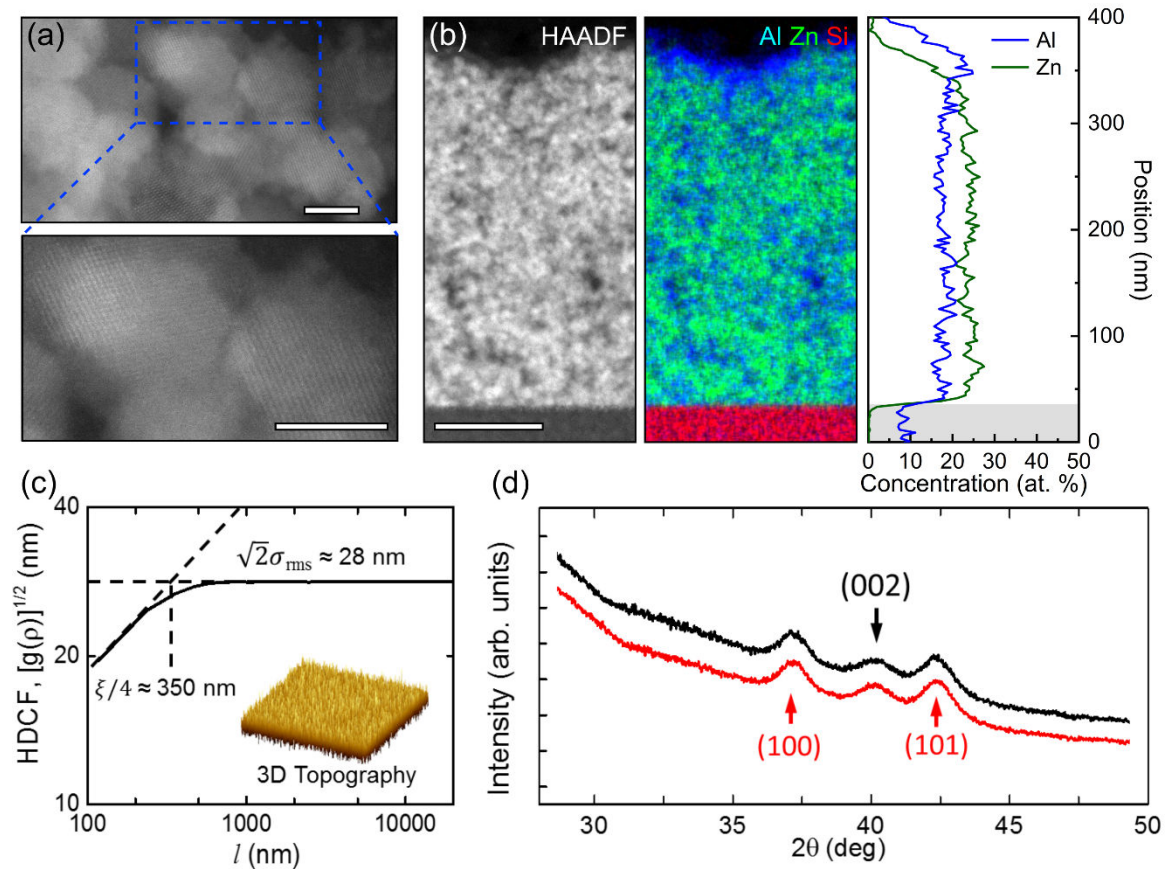
FIG. 2. Structural and surface characterization of ZnO NC networks: (a) A high-magnification HAADF-STEM image of sample 3-b along with atomic-resolution image of the highlighted (framed) region, which shows the structure of the interface between two NCs. Scale bars are 5 nm. (b) HAADF-STEM image and composite STEM-EDX map of the ZnO NCs film in cross section showing the distribution of elements throughout the film. The scale bar is 100 nm. The shaded region in the concentration distribution plot is the borosilicate glass substrate. (c) AFM HDCF and corresponding 3D topography (inset) over a 60-$\mu$m $\times$ 60-$\mu$m scanned area of sample 3-b. Dashed lines denote the extrapolations of the HDCF at small and large length scales for determining the in-plane correlation length ($\xi \approx 1.4$ $\mu$m) of the sample morphology ($\sigma_{rms} \approx 20$ nm). The height variation range of the 3D topography (inset) is 120 nm. (d) X-ray-scattering measurements of samples 3-a (red) and 3-b (black). The ZnO crystallite size estimated from diffraction patterns is the same for both samples.

A high-angle annular dark-field (HAADF)-STEM image of sample 3-b is depicted in Fig. 2(a), which shows that individual ZnO NCs are crystalline. A higher-magnification image of two ZnO NCs shows the inter-NC interface, a two-dimensional (2D) depiction of a 3D contact facet. Cross-sectional STEM-EDX maps and intensity profiles of the NC network [Fig. 2(b)] show that the Al$_2$O$_3$ fills the inter-NC voids uniformly throughout the thickness of the film. Si is chosen to visualize and distinguish the borosilicate substrate (amorphous SiO$_2$) since O atoms are also present in the ZnO NC network. Overall, sintering and doping IPL produce no detectable structural changes for all sample series.

Figure 2(c) shows a representative AFM image (inset) and the corresponding height-difference correlation function (HDCF) for sample 3-b, over a 60-$\mu$m $\times$ 60-$\mu$m area. The HDCF is defined as $g(l) = \langle (h_i - h_j)^2 \rangle$, an ensemble average in the height differences over pairs of locations $i$ and $j$ ($h_i$ and $h_j$) separated by a distance of $l$ [39]. The HDCF provides more information about the sample surface morphology than the rms roughness ($\sigma_{rms}$). From Fig. 2(c), two distinct regimes can be observed: a linear regime where $[g(l)]^{1/2}$ increases with $l$ and a saturated regime where $[g(l)]^{1/2}$ approaches $\sqrt{2}\sigma_{rms}$.

The in-plane correlation length scale $\xi$ is determined from the intersection of fits to the linear and saturated regimes. This gives $\xi \approx 1.4$ $\mu$m and $\sigma_{rms} \approx 20$ nm for these samples, suggesting the long-range surface uniformity and smoothness of these NC networks.

The representative XRD patterns from samples 3-a and 3-b are displayed in Fig. 2(d), which suggest that the ALD Al$_2$O$_3$ infill is amorphous in all samples and ZnO NC size does not change after infilling. The as-deposited NC size, determined from XRD peak widths (before infilling with ALD) is in the range of 9.2–9.6 nm [23,32]. For simplicity, we use 9.4 nm as the average for all samples. For sample series 2 and 3, it appears that some ALD ZnO infill deposits epitaxially on the NC surfaces, as we detect a slight increase in ZnO NC size after infilling with ZnO, compared to the as-deposited NCs without infill (e.g., an increase of 0.7 nm in sample 2-a and 2.6 nm in sample 3-a). The majority fraction of the ZnO infill in sample series 2 and 3 does not show any contribution to the crystalline diffraction of the samples.

Sintering IPL increases the contact radius $\rho$ by heating the NCs and inducing sintering. It also removes surface species, which facilitates additional sintering during the subsequent

Al$_2$O$_3$ ALD [23]. Without sintering IPL, the NC networks in-filled with Al$_2$O$_3$ via ALD have $\rho = 1.1$ nm. As the sintering IPL flashes increases from 0 to 1000, $\rho$ increases from 1.1 to 1.5 nm [23]. Doping IPL increases $n$ by removing residual electron-trapping surface species left over after Al$_2$O$_3$ ALD. Our previous study proposed that the key surface species that acted as traps were residual OH groups [23], although our more recent study raises the possibility that other species are also involved [32]. From Hall measurements, $n = 2.1 \times 10^{19}$ cm$^{-3}$ for sample 1-a, and 1000 flashes of doping IPL flashes increases $n$ to $4.8 \times 10^{19}$ cm$^{-3}$ for sample 1-b. Direct measurements of $n$ are currently unavailable for samples 2-a and 2-b and samples 3-a and 3-b. However, based on their $\sigma$ values and previous Hall measurements of similar samples [32], samples 2-a and 3-a most likely have $n$ similar to, or slightly lower than, that of sample 1-a ($5 \times 10^{18}$ cm$^{-3} < n < 2 \times 10^{19}$ cm$^{-3}$), while samples 2-b and 3-b likely have $n$ similar to or slightly greater than that of sample 1-b ($5 \times 10^{19}$ cm$^{-3} < n < 10^{20}$ cm$^{-3}$). As a result, through the combinations of sintering IPL and doping IPL treatments in all samples, the overall electrical conductivity $\sigma$ increases by several orders of magnitude (ranging from $\sim$0.03 to $\sim$150 $\Omega^{-1}$ cm$^{-1}$) [23,32], approaching or even crossing the metal-insulator-transition (MIT). Details of electrical conductivities are provided in Sec. S2 of the Supplemental Material [33].

## III. THERMAL CHARACTERIZATION

### A. Ultrafast thermal measurements

We apply time-domain thermoreflectance [TDTR, Fig. 1(a)], an ultrafast-laser based technique [40–44], to measure the thermal conductivities of ZnO NC networks ($\Lambda_{nw}$), and amorphous Al$_2$O$_3$ films ($\Lambda_{IF,Al2O3}$). Each sample is coated with an aluminum (Al) layer of $\approx$70 nm, which serves as a metal transducer. Prior to TDTR measurements, the thermal conductivity of the Al transducer is calibrated via four-point probe measurements coupled with the Wiedemann-Franz Law (WFL) estimates. For each sample we conduct TDTR measurements at two modulation frequencies (1.6 and 18 MHz), and obtain its thermal conductivity by simultaneously fitting two sets of dual-frequency TDTR data to a heat diffusion model [45]. The ultrafast TDTR experimental setup and details of the system can be found in previous publications [39,42,43,46].

### B. TDTR experimental results

Figure 3 shows representative TDTR data and the best fit to extract $\Lambda_{nw}$ for ZnO NC networks with different infill material compositions. The thickness of the Al transducer is calculated from the picosecond acoustics of the in-phase signal as shown in Fig. 3(a) [47]. Representative TDTR ratio signals ($-V_{in}/V_{out}$) acquired from different samples using the 18-MHz modulation frequency are shown as symbols in Fig. 3(b). Figure 3(c) depicts the TDTR data of sample 2-b measured at dual modulation frequencies (18 and 1.6 MHz). The red solid lines are the best-fit curves obtained by matching the heat diffusion model to TDTR measurements for the NC networks.
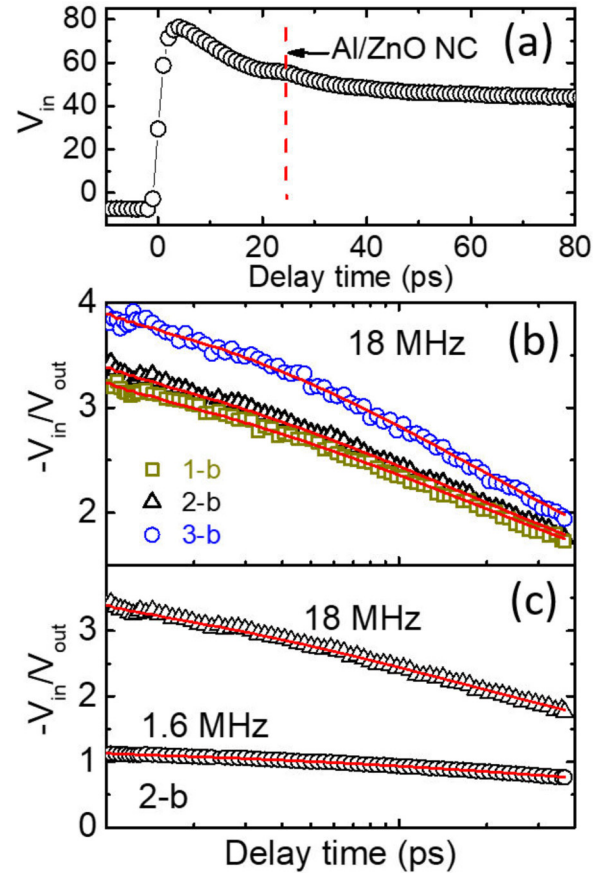


FIG. 3. (a) Picosecond acoustic signals from a representative ZnO NC sample to determine the Al thickness. (b) TDTR ratio signal and fitting results for ZnO NC networks after doping IPL treatments with different infill material compositions of ZnO and Al$_2$O$_3$. (c) TDTR ratio signal (symbols) and fitting results (red curves) at modulation frequencies of 18 and 1.6 MHz, respectively.

Measured network thermal conductivities $\Lambda_{nw}$ as well as the electronic thermal conductivity $\Lambda_e$ for three series (1–3) are shown in Fig. 4. The value of $\Lambda_e$ is converted from the in-plane electrical conductivity using WFL with the Sommerfeld value of Lorenz number ($L_0 = 2.44 \times 10^{-8}$ W $\Omega$ K$^{-2}$). As the sintering IPL flash number (red $x$ coordinate) increases, the electronic thermal conductivity $\Lambda_{1\_e}$ of series 1 (1-$m$-0, $m = 1$–1000) is enhanced by more than 2 orders of magnitude, due to the growth of contact radius $\rho$ between the NCs (from 1.1 to 1.5 nm) [23]. After the sintering IPL and ALD of infill materials, increasing the doping IPL pulses (blue $x$ coordinate, 11000-$n$, $n = 1$–1000) could further improve $\Lambda_{1\_e}$ because $n$ increases [23]. While IPL treatments could significantly enhance $\Lambda_e$ for the ZnO NCs infilled with Al$_2$O$_3$, the absolute value of $\Lambda_e$ is still negligible compared to $\Lambda_{nw}$ (more than two orders of magnitude smaller). We therefore conclude that the major contribution to $\Lambda_{nw}$ is from the phononic thermal conductivity.

Specific values of thermal conductivities and electronic thermal conductivities of sample series 1–3 (a and b) are included in Table II. At 1000 sintering IPL flashes and 0 doping IPL flashes, from samples 1-a to 3-a with increasing ZnO in the infill material (0, 23%, 76% in Al$_2$O$_3$ + ZnO infill
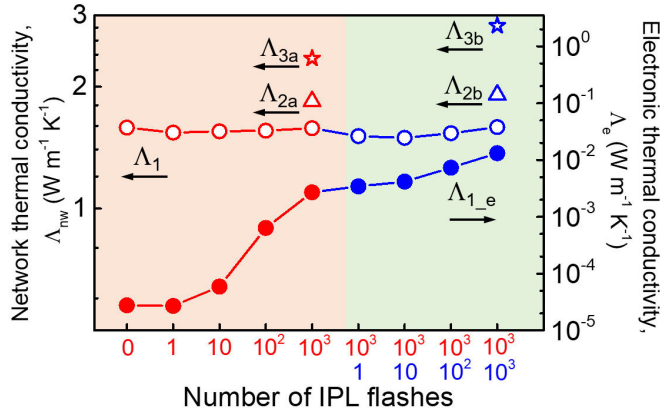
FIG. 4. Thermal conductivity of ZnO NCs with different annealing (red) and doping (blue) IPL flash numbers for series 1–3 (1: circles; 2: triangles; 3: stars). The open symbols and the solid symbols are the measured network thermal conductivity $\Lambda_{nw}$ and electronic thermal conductivity $\Lambda_e$, respectively. There are two $x$ coordinates, the first row with red numbers presents the sintering IPL flash numbers before ALD of infill materials, and the second row with blue numbers presents the doping IPL flash numbers after 1000 flashes of sintering IPL and ALD of infill materials.

by ALD), $\Lambda_{nw}$ increases monotonically by 49% from 1.58 to 2.35 W m$^{-1}$ K$^{-1}$. Such a monotonic increase suggests that adding more ZnO in the infill materials, rather than amorphous Al$_2$O$_3$, could enhance the overall thermal conductivity of ZnO NC networks.

Figure 4 shows that the network thermal conductivity $\Lambda_1$ for series 1 ($\sim$1.6 W m$^{-1}$ K$^{-1}$), is independent of sintering (i.e., increasing $\rho$) and doping IPL pulses (i.e., increasing $n$). This suggests that increasing $\rho$ has negligible impact on phononic thermal transport in series 1 (ZnO NC + Al$_2$O$_3$ infill), though increasing $\rho$ dramatically improves electronic transport [23]. Series 2 exhibits a similar trend ($\Lambda_2$, triangles), which has a larger fraction of Al$_2$O$_3$ (77%) and a smaller fraction of ZnO (23%) in the infill material (Al$_2$O$_3$ + ZnO infill). However, it is surprising to find that the 1000-doping IPL flashes could increase the thermal conductivity of series 3 ($\Lambda_3$, stars) by 20%, from 2.35 to 2.83 W m$^{-1}$ K$^{-1}$, which has

TABLE II. Measured $\Lambda_{nw}$ (presented as $\Lambda_1$, $\Lambda_2$, $\Lambda_3$ for sample series 1, 2, 3 in Fig. 4), and calculated electronic thermal conductivity $\Lambda_e$ for sample series 1–3. $\Lambda_e$ is converted from measured in-plane electrical conductivity through Wiedemann-Franz law, using the Sommerfeld value of the Lorenz number ($\Lambda_0 = 2.44 \times 10^{-8}$ W $\Omega$ K$^{-2}$). The sintering IPL flash number is 1000.

| Sample no. | IPL flashes after ALD (doping IPL) | $\Lambda_{nw}$ (W m$^{-1}$ K$^{-1}$) | $\Lambda_e$ (in-plane) (W m$^{-1}$ K$^{-1}$) |
|---|---|---|---|
| 1-a | 0 | 1.58 | 0.003 |
| 1-b | 1000 | 1.59 | 0.013 |
| 2-a | 0 | 1.84 | 0.004 |
| 2-b | 1000 | 1.91 | 0.03 |
| 3-a | 0 | 2.35 | 0.01 |
| 3-b | 1000 | 2.83 | 0.11 |

a similar infill composition as series 2 but different fractions (76% ZnO and 24%Al$_2$O$_3$). The corresponding phononic thermal conductivity of series 3, obtained from subtracting the in-plane electronic contribution from the measured $\Lambda_{nw}$, also increases by 16% from 2.34 to 2.71 W m$^{-1}$ K$^{-1}$, beyond our measurement uncertainty ($\sim$7–10%).

## IV. RESULTS AND DISCUSSION

### A. Modified effective-medium approximation (EMA) model

To better interpret the influences of different factors on thermal transport, we apply a modified effective-medium approximation (EMA) model to calculate the room-temperature NC network thermal conductivity ($\Lambda_{nw,cal}$) and compare with measurements. Conventional EMA models assume that isolated particles are dispersed in a continuous matrix [26,27,48,49]. This assumption is not valid in our samples because the NCs are formed in direct contact, a necessary condition for dramatically enhancing the electrical conductivity of NC networks [50]. Thus, we modify the EMA model to take into account the inter-NC contact radius and the NC-infill interfacial thermal conductance, following an approach developed in prior studies of aerogel [51,52]. Details about the modified EMA model are provided in Sec. S3 of the Supplemental Material [33].

The modified EMA model predictions are compared to the measured thermal conductivities of sample series 1–3. The comparison systematically reveals the influences of various factors on $\Lambda_{nw}$, including the NC thermal conductivity ($\Lambda_{NC}$) and volumetric fraction ($\varepsilon_{NC}$), the infill thermal conductivity ($\Lambda_{IF}$), the inter-NC contact radius ($\rho$), and the interfacial thermal conductance ($G$) between NCs and the infill material. For Sample series 1–3 with an NC diameter of $\sim$9.4 nm, we determine $\Lambda_{NC} = 8$ W m$^{-1}$ K$^{-1}$ by scaling down the bulk thermal conductivity of single-crystal ZnO ($\Lambda_{ZnO} = 50$ W m$^{-1}$ K$^{-1}$), based on the size effect from previous lattice dynamics calculations [53]. The use of the average NC diameter (9.4 nm), instead of the actual range of NC sizes (from 9.2 to 9.6 nm), makes a negligible difference ($<$1%) in the EMA predicted $\Lambda_{nw\_cal}$. Details are documented in Sec. S4 of the Supplemental Material [33]. The infill thermal conductivity is averaged over the thermal conductivities of individual components (Al$_2$O$_3$, pores, and/or ZnO) based on the corresponding volumetric fractions [49,54–56]. This gives $\Lambda_{IF} = 1.48$ W m$^{-1}$ K$^{-1}$ for sample series 1 composed of Al$_2$O$_3$ and pores (see details of $\Lambda_{IF}$ calculation in Sec. S3 of the Supplemental Material [33]). Additionally, as the sintering IPL pulses increase from 0 to 1000 in series 1, $\rho$ increases from 1.1 to 1.5 nm. By fitting the measured $\Lambda_{nw}$ of sample 1-a to the modified EMA model, we extract $G$ between the ZnO NC and Al$_2$O$_3$ infill to be 50M W m$^{-2}$ K$^{-1}$.

### B. Parametric sensitivity analysis

We conduct a further parametric sensitivity analysis, based on the modified EMA model, to examine the influence of individual parameters $\alpha$ ($\Lambda_{NC}$, $\varepsilon_{NC}$, $\Lambda_{IF}$, $\rho$, and $G$) on $\Lambda_{nw\_cal}$ (see Sec. S3 of the Supplemental Material [33]). For plotting purposes, we normalize the parameters to several reference values as specified in the caption of Fig. 5, which shows the
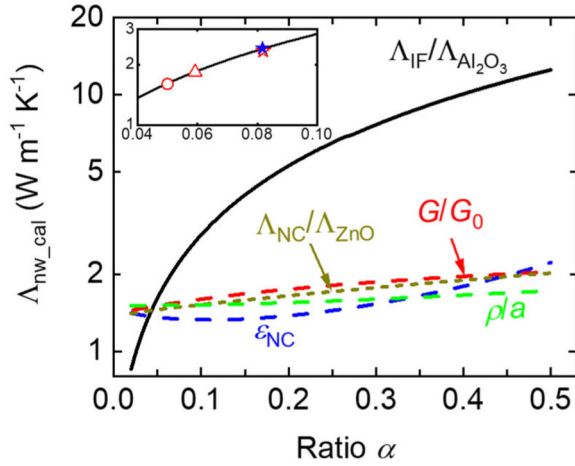
FIG. 5. The network thermal conductivity $\Lambda_{nw\_cal}$ as functions of various normalized parameters calculated from the modified EMA model, including $\Lambda_{NC}/\Lambda_{ZnO}$ (gold dashed line), $\Lambda_{IF}/\Lambda_{Al2O3}$ (black solid line), $G/G_0$ (red dashed line), $\rho/a$ (green dashed line). Specifically, $\Lambda_{NC}$ are normalized by the bulk thermal conductivity of single-crystal ZnO ($\Lambda_{ZnO} = 50$ W m$^{-1}$ K$^{-1}$) [52], $\Lambda_{IF}$ is normalized by the bulk thermal conductivity of single-crystal Al$_2$O$_3$ (sapphire, $\Lambda_{Al2O3} = 30$ W m$^{-1}$ K$^{-1}$) [57], $\rho$ is normalized by the NC radius ($a = 5$ nm), and $G$ is normalized by a reference value representing a good solid-solid thermal interface (e.g., $G_0 = 500$ M W m$^{-2}$ K$^{-1}$ between TiN and MgO) [58]. The inset shows the calculated $\Lambda_{nw\_cal}$ as a function of $\Lambda_{IF}/\Lambda_{Al2O3}$ in the range of 0.04–0.10, and the measured $\Lambda_{nw}$ for sample 1-a (open red circle), sample 2-a (open red triangle), and sample 3-a (open blue star) compared with the calculated $\Lambda_{nw}$ (solid blue star).

corresponding analysis. Overall, the analysis indicates that $\Lambda_{IF}$ is the dominant factor, $G$, $\Lambda_{NC}$, and $\varepsilon_{NC}$ have moderate impacts, and $\rho$ has the least impact on the network thermal conductivity. As we change the ratios of $\rho/a$, $\Lambda_{NC}/\Lambda_{ZnO}$, and $G/G_0$ from 0.1 to 0.5, the corresponding $\Lambda_{nw\_cal}$ increases by 13%, 33%, and 28%, respectively. The results demonstrate the independence of measured $\Lambda_{nw}$ (Fig. 4) on $\rho$ for sample series 1 after sintering IPL treatment, in which $\rho/a$ changes from 0.2 to 0.3 and our calculated $\Lambda_{nw\_cal}$ predicts an increase of only 4%. The moderate impact of $G$ is consistent with previous conclusions for dispersed NC composites [26,27].

We also find that the measured $\Lambda_{nw}$ of samples 1-a, 2-a, 3-a are smaller than the lower limit thermal conductivity calculated by assuming the serial thermal resistance networks of two constituents (NC and infill) without considering the influence of $G$. We conclude that network thermal conductivity ($\Lambda_{nw}$) is substantially suppressed by interfacial thermal resistance $G^{-1}$ (see details in Sec. S5 of the Supplemental Material [33]). It should be noted that our analysis shows a moderate impact of $\Lambda_{NC}$, which differs from previous calculations which concluded $\Lambda_{NC}$ had a negligible effect on $\Lambda_{nw}$ in dispersed NC composites [26,27]. We attribute this difference to the dense packing and unique direct-contact NC arrangement in our samples, which leads to a higher contribution to network conductivity, $\Lambda_{nw}$ by the NC heat transfer channel ($Q_2$ in Sec. S3 of the Supplemental Material [33]) compared to the dispersed NC composites.

It is interesting to find that as we change $\varepsilon_{NC}$ from 2% to 50%, $\Lambda_{nw\_cal}$ first decreases slightly (by ~6% until $\varepsilon_{NC} = 11\%$) and then increases (~67% until $\varepsilon_{NC} = 50\%$). We attribute this to two competing mechanisms: the high thermal conductivity of NCs ($\Lambda_{NC}$) and the low interfacial thermal conductance ($G$) between the NCs and the infill that becomes less important as $\varepsilon_{NC}$ increases and NC surface-to-volume ratio decreases (see details in Sec. S6 of the Supplemental Material [33]). Among all parameters varied in our work, the most dominant is the thermal conductivity of the infill material. As the ratio of $\Lambda_{IF}/\Lambda_{Al2O3}$ changes from 0.1 to 0.5, $\Lambda_{nw\_cal}$ increases significantly by 460% from ~ 2.8 W m$^{-1}$ K$^{-1}$ to ~13 W m$^{-1}$ K$^{-1}$

From TDTR measurements, $\Lambda_{nw}$ of sample 2-a is 1.84 W m$^{-1}$ K$^{-1}$ (open red triangle in the inset of Fig. 5), compared to 1.58 W m$^{-1}$ K$^{-1}$ (open red circle in the inset) of sample 1-a. We attribute this enhancement in $\Lambda_{nw}$ to an increase of $\Lambda_{IF}$ in sample 2-a, which has 21% ZnO infill compared to none in sample 1-a. Using the modified EMA model, we extract $\Lambda_{IF,ZnO} = 3$ W m$^{-1}$ K$^{-1}$ for sample 2-a. Furthermore, assuming the same value of $\Lambda_{IF,ZnO}$, we obtain $\Lambda_{nw\_cal} = 2.4$ W m$^{-1}$ K$^{-1}$ for sample 3-a (solid blue star in the inset) using the infill material compositions in Table I. The EMA-calculated $\Lambda_{nw}$ is in excellent agreement with the measured $\Lambda_{nw}$ for sample 3-a (2.35 W m$^{-1}$ K$^{-1}$, open blue star in the inset), with a deviation of only 2% within the typical TDTR measurement uncertainty (~7%).

### C. Phononic vs electronic contributions

Finally, we notice that the network thermal conductivity $\Lambda_{nw}$ measured via TDTR is 20% greater in sample 3-b (1000 doping IPL) compared to that of sample 3-a (no doping IPL), a sufficiently large contrast that can be distinguished by TDTR. We first suspected that the doping IPL may change the structure of the infilled ZnO. For example, IPL may crystallize amorphous portions of the ZnO infill and form epitaxially added layers on the NC surface. This may have affected the infill thermal conductivity substantially in sample 3-b compared to sample 3-a. To quantify the amount of crystallized ZnO infill, we estimate the ZnO crystallite size from XRD patterns [Fig. 2(c)]. The estimated ZnO crystallite size is 12 nm for both samples 3-a and 3-b, suggesting the 1000 doping IPL does not result in changes in crystallinity. Considering that the 1000 doping IPL flashes do not affect the structure of the infill amorphous Al$_2$O$_3$ [23], the above evaluation indicates that the phononic thermal conductivities should be the same for samples 3-a and 3-b.

We then hypothesize that the 20% enhancement in the through-plane $\Lambda_{nw}$ of sample 3-b is most likely resulting from the electronic contribution, i.e., a change of ~0.4 W m$^{-1}$ K$^{-1}$ in the through-plane electronic thermal conductivity ($\Lambda_{e\_th}$) as reflected in $\Lambda_{nw}$, before and after the IPL treatment. However, the in-plane electronic thermal conductivity ($\Lambda_{e\_in}$), directly converted from the measured in-plane electrical conductivity, is only ~0.1 W m$^{-1}$ K$^{-1}$ for sample 3-b (see Table II), which cannot fully explain the 20% enhancement. The comparison clearly shows that $\Lambda_{e\_th}$ of sample 3-b should be approximately four times larger than the WFL-derived $\Lambda_{e\_in}$. Sample 3-b is metallic [32] and the Lorenz number $L(\Lambda_e/\sigma = LT)$

for sample 3-b should not deviate from the Sommerfeld value, which is generally valid in metallic materials close to equilibrium [59,60]. Certain nondegenerate semiconductors [61–63] or insulators [64] exhibit an enhanced Lorenz number compared to the Sommerfeld value due to mechanisms such as the bipolar diffusion effect [61,62,64–67] and Dirac fluid effect [63,64]; however, such phenomena are unlikely in our samples, and have seldom been found in metallic materials [68].

We thus attribute the higher $\Lambda_{e\_th}$ compared to $\Lambda_{e\_in}$ to the anisotropy of electrical conductivities originating from the thin-film nature of sample 3-b. Specifically, in similar material systems [69,70], when the film thickness decreases to a very small value, some rare highly conductive paths, proposed by Miller and Abrahams [71] (MA), can dominate the charge transport along the through-plane direction rather than the usual percolation paths. In this case, the through-plane electrical conductivity (with MA paths dominant) can be significantly higher than that along the in-plane direction (with percolation paths dominant) [72,73]. Even though $\Lambda_{e\_th}$ ($\sim$ $0.4\,\mathrm{W\,m^{-1}\,K^{-1}}$) is much larger than $\Lambda_{e\_in}$ ($0.11\,\mathrm{W\,m^{-1}\,K^{-1}}$) for sample 3-b, the electronic contribution to the overall $\Lambda_{nw}$ ($2.83\,\mathrm{W\,m^{-1}\,K^{-1}}$) is less than 15%. Thus, we conclude that our statement that phonons are the dominant heat carriers in these ZnO NC networks is still valid.

## V. CONCLUSION

We have shown that by using two-phase heterogeneous nanocomposites, it is possible to independently control the electrical and thermal properties of a semiconductor film. The study has been carried out using plasma-synthesized, ligand-free, ZnO NC networks infilled with a:$Al_2O_3$ (and infill of a:ZnO-$a$:$Al_2O_3$ mix). We have demonstrated that the infill material provides the primary control over the thermal properties of these nanocomposites. Combining thermal conductivity measurements and a modified EMA model, we have found that infill thermal conductivity dominates the thermal conductivity of the entire network and, therefore, the thermal conductivity can be decoupled from electrical conductivity, which primarily depends on the NC contact radius ($\rho$) and the carrier concentration ($n$). While our experimental results demonstrate a tunability of $\Lambda_{nw}$ by nearly a factor of 2, the model predicts that the control of the network thermal conductivity can have an even wider range if different matrix (infill) materials are used, such as crystalline materials. The findings revealed in this work provide a pathway to explore new functional materials with independent control of thermal and electrical properties, which could be beneficial for a broad range of applications from solid-state energy converters to NC-based electronic devices.

## VI. EXPERIMENT

*Sample preparation.* ZnO NC networks were synthesized via nonthermal plasma synthesis and inertial impact deposition. These networks were infilled with ZnO and $Al_2O_3$ via ALD (Cambridge Nanotech/Ultratech Savannah S200), and sintered and photodoped by intense pulsed light (IPL) (Xenon Corp. Sinteron 2010 equipped with a 10-in. Xe U lamp). The treatment sequence was the following: 0–1000 flashes of sintering IPL, 0–32 cycles of ZnO ALD, 70 cycles of $Al_2O_3$ ALD, and then 0–1000 flashes of doping IPL.

*Characterization.* There were three sample series with different cycles of ZnO ALD, i.e., sample series 1–3 have 0, 8, 32 cycles of ZnO ALD, respectively (Table I). The samples were characterized by x-ray diffraction (XRD), analytical scanning STEM, and atomic force microscopy (AFM). The XRD measurements were done with a Bruker microdiffractometer equipped with a two-dimensional Vantec detector and a Co-$K_\alpha$ x-ray radiation point source ($\Lambda = 1.79\,$Å). The x-ray beam was conditioned with a graphite monochromator to avoid $K_\beta$ contributions to the scattering pattern. The x-ray-scattering data shown in this paper have been converted to the Cu-$K_\alpha$ wavelength ($\lambda = 1.54\,$Å). The crystallite size was determined by Scherrer analysis of the (100), (002), and (101) peaks of the ZnO NC XRD pattern using a shape factor of 0.9 $\times$ 4/3 to account for spheroidal morphology. Each peak was fitted to a single Gaussian profile, followed by the subtraction of the instrument broadening from each Gaussian profile's full width at half maximum to obtain the Scherrer broadening.

We prepared TEM cross-sectional lamellae using an FEI Helios NanoLab G4 dual-beam focused ion beam (FIB). The prepared lamellae were studied with STEM and energy-dispersive x-ray (EDX) spectroscopy in an FEI Titan G2 60–300 STEM equipped with a Super-X EDX spectrometer. High-angle annular dark-field (HAADF) STEM imaging was performed using a 200-kV beam with a probe convergence semiangle of 25 mrad. STEM-EDX maps were recorded using a 60-kV beam with a probe convergence semiangle of 25 mrad and a current of 120 pA. Spatially resolved STEM-EDX maps were collected using drift correction over a 520 nm by 520 nm area with 1024 pixels by 1024 pixels and dwell time of 4 μs/pixel. The intensities of Al, Zn, and Si $K$ edges were integrated after background-subtraction, producing a spectral image of the samples. A three-pixel Gaussian blur was applied to these STEM-EDX maps to aid visualization. The atomic concentrations of Zn, Al, Si, C, and O edges were quantified using Bruker Esprit 1.9 software package.

The surface morphology of samples was characterized by tapping-mode AFM (Keysight 5500). The values of electrical conductivity were characterized using the methods described previously and the results can be found in Sec. S2 of the Supplemental Material [33]. The volumetric fractions of ZnO NC and ZnO infill values were estimated from ellipsometry and Bruggeman effective-medium approximation detailed in prior studies [23,32]. For series 3, the volumetric fractions of ZnO infill were extrapolated from the measurements of series 1 and 2, using Thimsen's geometrical model [20]. In addition, a simple geometrical model was used to translate changes in volume fraction to changes in $\rho$ [23]. $Al_2O_3$ volume fraction was estimated by assuming that the total solid volume fraction (ZnO + $Al_2O_3$) is 95%, based on a previous study of the dependence of volume fraction of ZnO-infilled ZnO on the number of ZnO ALD cycles [20].

[1] D. G. Cahill, K. Goodson, and A. Majumdar, J. Heat Transfer **124**, 223 (2002).

[2] A. Minnich, M. Dresselhaus, Z. Ren, and G. Chen, Energy Environ. Sci. **2**, 466 (2009).

[3] B. Poudel, Q. Hao, Y. Ma, Y. Lan, A. Minnich, B. Yu, X. Yan, D. Wang, A. Muto, D. Vashaee *et al.*, Science **320**, 634 (2008).

[4] G. Joshi, H. Lee, Y. Lan, X. Wang, G. Zhu, D. Wang, R. W. Gould, D. C. Cuff, M. Y. Tang, M. S. Dresselhaus *et al.*, Nano Lett. **8**, 4670 (2008).

[5] X. W. Wang, H. Lee, Y. C. Lan, G. H. Zhu, G. Joshi, D. Z. Wang, J. Yang, A. J. Muto, M. Y. Tang, J. Klatsky *et al.*, Appl. Phys. Lett. **93**, 193121 (2008).

[6] Y. Lan, A. J. Minnich, G. Chen, and Z. Ren, Adv. Funct. Mater. **20**, 357 (2010).

[7] W. W. Yu, L. Qu, W. Guo, and X. Peng, Chem. Mater. **15**, 2854 (2003).

[8] L. Brus, J. Phys. Chem. **90**, 2555 (1986).

[9] J.-S. Lee, M. V. Kovalenko, J. Huang, D. S. Chung, and D. V. Talapin, Nat. Nanotechnol. **6**, 348 (2011).

[10] C. B. Murray, C. R. Kagan, and M. G. Bawendi, Science **270**, 1335 (1995).

[11] C. Burda, X. Chen, R. Narayanan, and M. A. El-Sayed, Chem. Rev. **105**, 1025 (2005).

[12] I. Gur, N. A. Fromer, M. L. Geier, and A. P. Alivisatos, Science **310**, 462 (2005).

[13] X. Lan *et al.*, Nano Lett. **16**, 4630 (2016).

[14] V. Wood and V. Bulović, Nano Rev. **1**, 5202 (2010).

[15] X. Dai, Z. Zhang, Y. Jin, Y. Niu, H. Cao, X. Liang, L. Chen, J. Wang, and X. Peng, Nature (London) **515**, 96 (2014).

[16] J.-H. Choi *et al.*, Science **352**, 205 (2016).

[17] M. E. Turk, J.-H. Choi, S. J. Oh, A. T. Fafarman, B. T. Diroll, C. B. Murray, C. R. Kagan, and J. M. Kikkawa, Nano Lett. **14**, 5948 (2014).

[18] M. Ibáñez *et al.*, Nat. Commun. **7**, 10766 (2016).

[19] M. V. Kovalenko, B. Spokoyny, J.-S. Lee, M. Scheele, A. Weber, S. Perera, D. Landry, and D. V. Talapin, J. Am. Chem. Soc. **132**, 6686 (2010).

[20] E. Thimsen, M. Johnson, X. Zhang, A. J. Wagner, K. A. Mkhoyan, U. R. Kortshagen, and E. S. Aydil, Nat. Commun. **5**, 5822 (2014).

[21] M. Groner, F. Fabreguette, J. Elam, and S. George, Chem. Mater. **16**, 639 (2004).

[22] B. L. Greenberg, S. Ganguly, J. T. Held, N. J. Kramer, K. A. Mkhoyan, E. S. Aydil, and U. R. Kortshagen, Nano Lett. **15**, 8162 (2015).

[23] B. L. Greenberg, Z. L. Robinson, K. V. Reich, C. Gorynski, B. N. Voigt, L. F. Francis, B. I. Shklovskii, E. S. Aydil, and U. R. Kortshagen, Nano Lett. **17**, 4634 (2017).

[24] M. Law, L. E. Greene, A. Radenovic, T. Kuykendall, J. Liphardt, and P. Yang, J. Phys. Chem. B **110**, 22652 (2006).

[25] U. R. Kortshagen, R. M. Sankaran, R. N. Pereira, S. L. Girshick, J. J. Wu, and E. S. Aydil, Chem. Rev. **116**, 11061 (2016).

[26] W. L. Ong, S. M. Rupich, D. V. Talapin, A. J. H. McGaughey, and J. A. Malen, Nat. Mater. **12**, 410 (2013).

[27] M. Liu, Y. Ma, and R. Y. Wang, ACS Nano **9**, 12079 (2015).

[28] P. Ruckdeschel and M. Retsch, Adv. Mater. Interfaces **4**, 1700963 (2017).

[29] W.-L. Ong, S. Majumdar, J. A. Malen, and A. J. H. McGaughey, J. Phys. Chem. C **118**, 7288 (2014).

[30] M. B. Zanjani and J. R. Lukes, J. Appl. Phys. **115**, 143515 (2014).

[31] T. Chen, K. V. Reich, N. J. Kramer, H. Fu, U. R. Kortshagen, and B. I. Shklovskii, Nat. Mater. **15**, 299 (2016).

[32] B. L. Greenberg, Z. L. Robinson, Y. Ayino, J. T. Held, T. A. Peterson, K. A. Mkhoyan, V. S. Pribiag, E. S. Aydil, and U. R. Kortshagen, Sci. Adv. **5**, eaaw1462 (2019).

[33] See Supplemental Material at http://link.aps.org/supplemental/10.1103/PhysRevMaterials.4.086001 for details regarding the list of nomenclatures, electrical conductivity, structural parameters, and the derivations and discussions about the EMA modeling.

[34] L. Mangolini, E. Thimsen, and U. Kortshagen, Nano Lett. **5**, 655 (2005).

[35] N. Rao, H. Lee, M. Kelkar, D. Hansen, J. Heberlein, P. H. McMurry, and S. L. Girshick, Nanostruct. Mater. **9**, 129 (1997).

[36] N. Rao, N. Tymiak, J. Blum, A. Neuman, H. Lee, S. L. Girshick, P. H. McMurry, and J. Heberlein, J. Aerosol Sci. **29**, 707 (1998).

[37] Z. C. Holman and U. R. Kortshagen, Nanotechnology **21**, 335302 (2010).

[38] D. Lanigan and E. Thimsen, ACS Nano **10**, 6744 (2016).

[39] X. Wang, V. Ho, R. A. Segalman, and D. G. Cahill, Macromolecules **46**, 4937 (2013).

[40] X. Wu, Y. Ni, J. Zhu, N. D. Burrows, C. J. Murphy, T. Dumitrica, and X. Wang, ACS Appl. Mater. Interfaces **8**, 10581 (2016).

[41] J. Zhu, Y. Zhu, X. Wu, H. Song, Y. Zhang, and X. Wang, Appl. Phys. Lett. **108**, 231903 (2016).

[42] J. Zhu, X. Wu, D. M. Lattery, W. Zheng, and X. Wang, Nanosc. Microsc. Therm. **21**, 177 (2017).

[43] X. Wu *et al.*, Adv. Funct. Mater. **27**, 1704233 (2017).

[44] J. Zhu, T. Feng, S. Mills, P. Wang, X. Wu, L. Zhang, S. T. Pantelides, X. Du, and X. Wang, ACS Appl. Mater. Interfaces **10**, 40740 (2018).

[45] D. G. Cahill, Rev. Sci. Instrum. **75**, 5119 (2004).

[46] X. Wang, C. D. Liman, N. D. Treat, M. L. Chabinyc, and D. G. Cahill, Phys. Rev. B **88**, 075310 (2013).

[47] G. T. Hohensee, W.-P. Hsieh, M. D. Losego, and D. G. Cahill, Rev. Sci. Instrum. **83**, 114902 (2012).

[48] A. Minnich and G. Chen, Appl. Phys. Lett. **91**, 073105 (2007).

[49] J. Wang, J. K. Carson, M. F. North, and D. J. Cleland, Int. J. Heat Mass Transf. **49**, 3075 (2006).

[50] W. J. Baumgardner, K. Whitham, and T. Hanrath, Nano Lett. **13**, 3225 (2013).

[51] G. Wei, Y. Liu, X. Zhang, F. Yu, and X. Du, Int. J. Heat Mass Transf. **54**, 2355 (2011).

[52] S. O. Zeng, A. Hunt, and R. Greif, J. Heat Transfer **117**, 1055 (1995).

[53] X. Wu, J. Lee, V. Varshney, J. L. Wohlwend, A. K. Roy, and T. Luo, Sci. Rep. **6**, 22504 (2016).

[54] S.-M. Lee, D. G. Cahill, and T. H. Allen, Phys. Rev. B **52**, 253 (1995).

[55] C. S. Gorham, J. T. Gaskins, G. N. Parsons, M. D. Losego, and P. E. Hopkins, Appl. Phys. Lett. **104**, 253107 (2014).

[56] T. L. Bergman, F. P. Incropera, D. P. DeWitt, and A. S. Lavine, *Fundamentals of Heat and Mass Transfer* (John Wiley & Sons, New York, 2011).

[57] D. G. Cahill, S.-M. Lee, and T. I. Selinder, J. Appl. Phys. **83**, 5783 (1998).

[58] H.-K. Lyeo and D. G. Cahill, Phys. Rev. B **73**, 144301 (2006).

[59] G. K. White, in *Thermal Conductivity of Pure Metals and Alloys*, Vol. L.B. 15c, edited by O. Madelung and G. K. White (Springer-Verlag, Berlin, 1991), p.107.

[60] V. Palenskis, World Journal of Condensed Matter Physics **3**, 73 (2013).

[61] T. Takeuchi, Z. Kristallogr. Cryst. Mater. **224**, 35 (2009).

[62] J.-S. Rhyee, E. Cho, K. Ahn, K. H. Lee, and S. M. Lee, Appl. Phys. Lett. **97**, 152104 (2010).

[63] J. Crossno *et al.*, Science **351**, 1058 (2016).

[64] Z. Luo, J. Tian, S. Huang, M. Srinivasan, J. Maassen, Y. P. Chen, and X. Xu, ACS Nano **12**, 1120 (2018).

[65] M. T. Pettes, J. Maassen, I. Jo, M. S. Lundstrom, and L. Shi, Nano Lett. **13**, 5316 (2013).

[66] B.-L. Huang and M. Kaviany, Phys. Rev. B **77**, 125209 (2008).

[67] A. Weathers, Z. U. Khan, R. Brooke, D. Evans, M. T. Pettes, J. W. Andreasen, X. Crispin, and L. Shi, Adv. Mater. **27**, 2101 (2015).

[68] C. Castellani, C. DiCastro, G. Kotliar, P. A. Lee, and G. Strinati, Phys. Rev. Lett. **59**, 477 (1987).

[69] J. J. Hauser, Phys. Rev. Lett. **29**, 476 (1972).

[70] J. J. Hauser and A. Staudinger, Phys. Rev. B **8**, 607 (1973).

[71] A. Miller and E. Abrahams, Phys. Rev. **120**, 745 (1960).

[72] M. Pollak and J. J. Hauser, Phys. Rev. Lett. **31**, 1304 (1973).

[73] M. E. Raikh and I. M. Ruzin, Pis'ma Zh. Eksp. Teor. Fiz. **43**, 437 (1986) [JETP Lett. **43**, 562 (1986)].